



### Science Arts & Métiers (SAM)

is an open access repository that collects the work of Arts et Métiers Institute of Technology researchers and makes it freely available over the web where possible.

This is an author-deposited version published in: <https://sam.ensam.eu>  
Handle ID: <http://hdl.handle.net/10985/23582>



This document is available under CC BY-NC-ND license

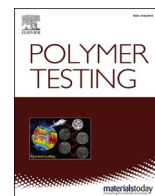
#### To cite this version :

Sara ZANCHI, Marie ENGEL, Antoine PASCAUD, François BARGAIN, Sylvie LEBRETON, Fabrice DOMINGUE DOS SANTOS, Sébastien ROLAND, Sylvie TENCE-GIRAULT - Unraveling the morphological diversity of P(VDF-ter-TrFE-ter-CTFE) semi-crystalline terpolymers via combined AFM and SAXS experiments - Polymer Testing - Vol. 120, p.107973 - 2023

Any correspondence concerning this service should be sent to the repository

Administrator : [scienceouverte@ensam.eu](mailto:scienceouverte@ensam.eu)





# Unraveling the morphological diversity of P(VDF-*ter*-TrFE-*ter*-CTFE) semi-crystalline terpolymers via combined AFM and SAXS experiments

Sara Zanchi<sup>a</sup>, Marie Engel<sup>a</sup>, Antoine Pascaud<sup>a</sup>, François Bargain<sup>b</sup>, Sylvie Lebreton<sup>b</sup>, Fabrice Domingues dos Santos<sup>c</sup>, Sébastien Roland<sup>a,\*</sup>, Sylvie Tencé-Girault<sup>a,b,\*</sup>

<sup>a</sup> Laboratoire PIMM, Arts et Metiers Institute of Technology, CNRS, Cnam, HESAM Université, 151 Boulevard de l'Hopital, 75013, Paris, France

<sup>b</sup> Arkema, CERDATO, Route du Rilsan, 27470, Serquigny, France

<sup>c</sup> Piezotech S.A.S, Arkema - CRRA, rue Henri Moissan, 69493, Pierre-Bénite Cedex, France

## ARTICLE INFO

### Keywords:

Morphology  
VDF based terpolymer  
AFM  
SAXS  
Crystallization

## ABSTRACT

In this article, the diverse morphologies observed after annealing or crystallization from the melt in P(VDF-*ter*-TrFE-*ter*-CTFE) terpolymers with varying CTFE amounts were explained through a combination of AFM and SAXS experiments. The very significant and, so far, unexplained evolution of the SAXS spectra after annealing above the Curie transition was interpreted by the formation, during annealing, of semi-crystalline domains without a significant evolution of the crystalline lamellar period. The morphologies obtained after crystallization from the melt were also explained and the coexistence of two periodic stacks (with period around 30–40 nm and 14–18 nm) was shown. Low cooling rates and CTFE amounts create long and thick semi-crystalline domains with a well-defined orientation, while high cooling rates and CTFE amounts create thinner and shorter domains, without a predominant orientation. The AFM images showed that the periodic organization of the crystalline lamellae with a period,  $L_p$ , around 15 nm is maintained, regardless of the crystallization process used (solvent cast, annealed, or melt-crystallized). The combined AFM/SAXS method used in this study can be applied to other semi-crystalline polymers.

## 1. Introduction

Poly(vinylidene fluoride-co-trifluoroethylene) (P(VDF-*co*-TrFE)) copolymers and poly(vinylidene fluoride-*ter*-trifluoroethylene-*ter*-chlorotrifluoroethylene) (P(VDF-*ter*-TrFE-*ter*-CTFE)) terpolymers are semi-crystalline fluorinated electroactive polymers. They have been widely studied in the last decades because of their numerous applications in many fields related to flexible organic electronics [1], such as actuators [2,3], sensors [4,5], memory devices [6,7], and energy harvesters [8,9].

The origin of P(VDF-*co*-TrFE) and P(VDF-*ter*-TrFE-*ter*-CTFE) electroactive properties mainly lies on the high polarity of C–F bonds, which induces strong dipolar moments perpendicularly to the polymer chain. Dipoles belonging to the crystal fraction are primarily responsible for the electroactive properties of these polymers [10]. In P(VDF-*co*-TrFE) copolymers, the presence of TrFE monomers induces all-*trans* conformations along the polymer chains, enabling the formation of large FerroElectric (FE) domains. For P(VDF-*ter*-TrFE-*ter*-CTFE) terpolymers,

the added termonomer CTFE, bulkier and carrying a weaker dipole than VDF and TrFE [11], induces the incorporation of *Gauche* conformations in the all-*trans* sequences. The addition of this termonomer, less mobile under an electric field, breaks the dipoles sequences, and leads to Relaxor-FerroElectric (RFE) behavior. These copolymers and terpolymers exhibit a Curie or pseudo-Curie transition to the high temperature ParaElectric (PE) phase [12–16]. Many publications describe the crystalline phases, Low Temperature (LT) or FE, DFE (Defective FerroElectric), RFE, and High Temperature (HT) or PE and the phase diagrams of these various copolymers and terpolymers [13,17,18].

These semi-crystalline copolymers are peculiar and fascinating for various reasons. First, the TrFE and VDF monomers are isomorphic, thus the TrFE incorporates into the all-*trans* crystal lattice of PVDF [19,20], extending only slightly the crystalline cell. Similarly, the CTFE monomer incorporates into the crystal lattice of P(VDF-*co*-TrFE) [21]. Second, the spherulitic morphology usually observed in PVDF is destroyed by the incorporation of the TrFE monomer [22]. To our knowledge, no

\* Corresponding author. Laboratoire PIMM, Arts et Metiers Institute of Technology, CNRS, Cnam, HESAM Université, 151 Boulevard de l'Hopital, 75013, Paris, France.

\*\* Corresponding author.

E-mail addresses: [sebastien.roland@ensam.eu](mailto:sebastien.roland@ensam.eu) (S. Roland), [sylvie.girault@ensam.eu](mailto:sylvie.girault@ensam.eu) (S. Tencé-Girault).

<https://doi.org/10.1016/j.polymeresting.2023.107973>

Received 27 January 2023; Received in revised form 17 February 2023; Accepted 27 February 2023

Available online 2 March 2023

0142-9418/© 2023 The Authors. Published by Elsevier Ltd. This is an open access article under the CC BY-NC-ND license (<http://creativecommons.org/licenses/by-nc-nd/4.0/>).

observation of spherulites has been reported for these copolymers. Finally, due to the Curie transition, annealing treatment is performed in the high temperature phase (PE). Annealing induces both a significant increase in crystallinity, but also a modification of the crystalline phases ratios (FE/DFE or FE/RFE), and a modification of the morphology [18, 23].

Morphological studies of these copolymers have appeared in recent years, based on electron microscopy [2,24,25], Atomic Force Microscopy (AFM) [26–30], and Small Angle X-ray Scattering (SAXS) experiments [16,23,31,32]. Indeed, these non-spherulitic morphologies, qualified as grain, needle or fiber microstructures [2,24–29,33,34] are unusual. Moreover, these studies give access to the orientation of the crystalline domains and therefore of the chains carrying the dipoles. The control of this orientation is essential to optimize the electroactive properties of these copolymers [24,28,35].

The evolutions of the SAXS signal after annealing or during a temperature cycle are very significant. The shift of the SAXS signal towards very small angles is interpreted as an unprecedented and unexplained increase in the long period ( $L_p$ ) [15,23,31,36], while the intensity variations are interpreted by considering the changes in electron densities due to the crystal phase changes [16].

Most of AFM existing studies focused on P(VDF-co-TrFE) films and investigated the crystalline morphology after various thermal treatments, below, at, and above the melting temperature [26–30]. The morphology of annealed P(VDF-co-TrFE) thin films has been described in the literature as homogeneously distributed rice-like domains, consisting of stacks of lamellae [30]. Hafner et al. observed by AFM that the well-ordered polymer chains are arranged in platelet-like crystalline lamellae [30]. The gap between each pair of lamellae is made of disordered polymer chain conformations, which lead to the amorphous interlamellar regions of the rice-like domains [30]. It is known that thermal treatments above the melting temperature of P(VDF-co-TrFE) thin films induce the crystallization of larger and longer needle-like structures [26–29]. The morphology and the orientation of these crystalline domains have been studied by coupling AFM and GIWAXD (Grazing Incident Wide Angle X-ray Diffraction) analyses [27]. Polymer chains have a preferential orientation perpendicular to the substrate, leading to extended « flat-on » crystalline domains, but also some « edge-on » (needle-like in AFM images) domains are observed. However, the AFM image scale was too large to adequately discern the internal structure of the crystal domains [27]. This AFM morphological study is the only one mentioning the effect of the cooling rate from the melt, which plays a key role in the crystallization kinetics. A comparison between a quenched and a slowly cooled copolymer thin film was performed, showing that the partial « edge-on » orientation and stacking of crystalline lamellae disappears for the quenched sample [27]. Otherwise, the existing AFM literature about P(VDF-co-TrFE) thin films morphology rarely gives an exhaustive interpretation. The morphology after crystallization from the melt was also described as crystalline « rods » and « fibers », which consist of chains extended in the same direction of the crystalline structure [26]. The authors did not mention the amorphous phase, nor the internal lamellar structure of the observed crystalline objects. The « needles » crystallized from the melt were also described elsewhere as the crystalline lamella [28]. This shows that many interpretations exist for the melt/crystallized morphologies, and they are often contradictory and unclear. Therefore, a study clarifying and understanding these morphologies is still missing. In addition, to the best of our knowledge, there is no exhaustive AFM study on the P(VDF-ter-TrFE-ter-CTFE) terpolymer films morphology [35].

Studies coupling SAXS and AFM observations show interesting results for polyelectrolytes [37], to understand the crystalline lamellae evolution with thermal treatments [38–40], to study the nanostructuration of block copolymers [41–43]. However, SAXS and AFM studies have scarcely been combined for fluorinated copolymers [44], which is the goal of the present study. We think that the combination of SAXS and AFM studies could explain the significant changes in

morphologies observed after thermal treatments.

On the one hand, the SAXS analysis provides information on the organization of different domains characterized by different electron density (for example crystalline and amorphous), with characteristic lengths ranging from one to a few hundred nanometers. SAXS experiments give information averaged over a large volume (around  $10^6 \mu\text{m}^3$ ) representative of the entire sample. Their interpretations can be intricate if the lamellae stack differently compared to the simplistic crystal/amorph model [38–40,45].

On the other hand, AFM images are performed on spin-coated thin films (around 100 nm) and the scanned area is only around few  $\mu\text{m}^2$ . This local information at the surface of the sample is topographic and/or related to the mechanical modulus. However, provided that the contrast conditions are optimized for imaging, it is possible to clearly distinguish crystalline and amorphous domains.

The comparison of these two methods (SAXS and AFM) is therefore not obvious. First of all, one can wonder if the same morphologies can be created in a thin spin-coated film and in a thick bar-coated film. Then, the dimensions measured on the surface by AFM and averaged in the volume using SAXS are not necessarily comparable. Since the answers to these questions are not obvious, a specific experimental procedure was adopted in this study. By varying a single parameter at a time, the morphological evolutions induced by this parameter were followed, on the one hand, on the AFM observations and, on the other hand, on the SAXS spectra. These changes observed either with AFM or by SAXS were then analyzed in parallel. It is the correlation between these evolutions that is discussed and interpreted. To analyze and interpret the unconventional SAXS signals, we explore the use of a phenomenological peak-fitting method, as previously reported in the literature [46–48], to separate various contributions in the SAXS correlation peak.

In this paper, we assessed the effect of processing conditions and of the chemical composition (0–10 %CTFE) on the crystalline morphologies for P(VDF-ter-TrFE-ter-CTFE) terpolymers, with a particular focus on the effect of the cooling rate from the melt on the stacking of crystalline lamellae, their orientation and their dimensions. By applying the method previously described, the chemical composition, the thermal treatment, and the cooling rate were successively used as variable parameters. The induced morphological evolutions were followed by the two aforementioned techniques. Very interesting conclusions on the morphological evolution of these copolymers were deduced. As an example, it was possible to understand why the SAXS signal shifts so much and irreversibly towards small angles after annealing, thus answering questions that have remained unanswered in the literature [31]. To better understand the evolutions of morphology, in-situ temperature experiments were also performed, both by AFM and SAXS.

## 2. Experimental part

### 2.1. Materials and samples preparation

A P(VDF-co-TrFE) 65/35 mol % copolymer and four P(VDF-ter-TrFE-ter-CTFE) terpolymers ranging from 4 to 10 mol % CTFE powders were provided by Piezotech. Samples were named TerpoX-Y, where X refers to the VDF/(TrFE + VDF) ratio and Y to the amount of CTFE (mol %) (see Table 1). Polymer powders were dissolved in methylethylketone at 14 wt % by using a reflux set-up at 80 °C for 3 h to get homogeneous

**Table 1**

List of the samples.

Name	VDF/(VDF + TrFE) mol %	CTFE mol %	T <sub>m</sub> (°C)
Terpo65-0	65	0	150
Terpo66-4.7	66	4.7	135
Terpo67-6.4	67	6.4	125
Terpo67-8.3	67	8.3	115
Terpo68-10.3	68	10.3	110

polymer solution. Solutions were then filtered with a 0.6  $\mu\text{m}$  mesh filter in order to remove any impurity. Depending on the analysis, two different techniques were used for the preparation of the samples, namely bar-coating and spin-coating.

### 2.1.1. Bar-coating

The polymer solution was uniformly spread on a glass substrate thanks to a bar-coater and left 30 min at room temperature, to let the solvent evaporate and to get 20  $\mu\text{m}$  thick solvent-cast films. Two different thermal treatments were performed on these films in an oven: an annealing treatment and a melting/crystallization treatment. The treatments temperatures are defined in relation to the melting temperature  $T_m$ . The former was performed at  $T_m - 15^\circ\text{C}$  for 1 h, the latter was performed by cooling after an isotherm at  $T_m + 25^\circ\text{C}$  for 15 min. In both cases, the oven was turned off after the thermal treatment and the door was left partially open, in order to slowly cool the polymer films to room temperature. The solvent-cast, annealed, and melt-crystallized terpolymer films were named TerpoX-Y-SC, TerpoX-Y-A, and TerpoX-Y-MC, respectively. These samples were used to perform SAXS experiments, in order to understand the effect of the thermal treatment and composition.

### 2.1.2. Spin-coating

A silicon wafer, cleaned with piranha solution ( $\text{H}_2\text{SO}_4:\text{H}_2\text{O}_2$ , 3:1) for 1 h, was used as a substrate. The polymer solution was diluted to 2 wt% and spin-coated at 2000 rpm rotational speed for 60 s. The solvent evaporated during the spin-coating, leaving a 100 nm thick film. Two different thermal treatments were performed in a Linkam THMS600 heating stage. The annealing was done at  $T_m - 15^\circ\text{C}$  for 1 h, using  $10^\circ\text{C}/\text{min}$  as heating and cooling ramps. The melting/crystallization treatment consisted in melting the film at  $T_m + 25^\circ\text{C}$  for 15 min, followed by a cooling at different rates ranging from  $1^\circ\text{C}/\text{min}$  to  $100^\circ\text{C}/\text{min}$ . These terpolymer samples, annealed and melt-crystallized with a controlled cooling rate ( $r$ ) were named TerpoX-Y-A10 and TerpoX-Y-MCr, respectively. For example, Terpo67-6.4-MC10, is a film melt-crystallized at a cooling rate of  $10^\circ\text{C}/\text{min}$ , prepared with the terpolymer having a molar ratio  $\text{VDF}/(\text{VDF} + \text{TrFE}) = 67 \text{ mol}\%$  and 6.4 mol% of CTfE.

## 2.2. Atomic Force Microscopy (AFM)

A Multimode 8 (Bruker) microscope controlled by a Nanoscope V controller and operating in the PeakForce QNM mode was used, in order to avoid possible surface damages due to the tip contact. ScanAsyst-Air-HR cantilevers with a nominal frequency of 130 kHz, a nominal spring constant of 0.4 N/m, and a nominal tip radius of 2 nm were used. Topography and mechanical images were analyzed, in order to characterize the morphologies of the different samples. For high temperature in-situ AFM analyses, Tapping mode<sup>®</sup> was used with ScanAsyst-Air cantilevers with a nominal frequency, spring constant and tip radius of 70 kHz, 0.4 N/m, and 2 nm, respectively. The sample (Terpo65-0 film) was heated from room temperature until the annealing temperature ( $130^\circ\text{C}$ ) with plateaus (ca. 10 min) at intermediate temperatures to allow the in-situ AFM imaging. At  $130^\circ\text{C}$ , a 1 h in-situ annealing was finally performed, then the sample was cooled back to room temperature.

## 2.3. Small angles X-ray scattering (SAXS)

Small Angle X-rays Scattering experiments were performed on a Xenocs Nano-inXider SW system in transmission mode using Cu K $\alpha$  radiation ( $\lambda = 1.54 \text{ \AA}$ ) from an X-ray microsource (GeniX3D) operating at 50 kV-0.6 mA (30 W). Scattering patterns were collected using a Pilatus3 (Dectris) detector. The collimation was chosen to maximize the intensity while adjusting the  $q$  range to the studied samples. The  $q$  range is between  $0.01 \text{ \AA}^{-1}$  and  $0.35 \text{ \AA}^{-1}$ . The reduction of 2D datasets from the Pilatus3 detector to 1D was achieved by radially averaging the raw data

detector counts using Foxtrot data reduction software. Then, SAXS spectra were normalized by the acquisition time and by the number of transmitted photons.

The 20  $\mu\text{m}$  thick solvent-cast films (SC) were studied at room temperature as well as during heating up to the annealing temperature. The acquisition time was set at 600 s for static experiments and at 60 s for in-situ experiments during heating ramp. For the in-situ thermal experiments, 20  $\mu\text{m}$  thick films were put in between two aluminum foils in a Linkam hot stage (HFSX350) and submitted to thermal ramps (rate  $10^\circ\text{C}/\text{min}$ ) having plateaus every  $5^\circ\text{C}$  to enable SAXS data acquisitions. After stabilizing the temperature, the SAXS patterns were recorded during 60 s at each defined temperature.

SAXS experiments were also carried out on the SWING beamline at the Soleil synchrotron facility (project n $^\circ$ : 20210035). The beam energy was set at 10 keV, leading to a wavelength of  $1.24 \text{ \AA}$ . SAXS patterns were recorded using an EigerX4M detector (Dectris) at 4.29 m from the sample, leading to a  $q$  range between  $0.002 \text{ \AA}^{-1}$  and  $0.24 \text{ \AA}^{-1}$ . This beamline allowed us to perform in-situ experiments during thermal cycles at different cooling rates with low acquisition times and a good signal for annealed (-A) and melt crystallized (-MC) samples. For static experiments, the acquisition time was set to 2 s and to 200 ms for in-situ experiments during temperature cycles. The reduction of 2D pattern from the Eiger detector to 1D was achieved by radially averaging the 2D images using Foxtrot software. Then, SAXS spectra were normalized by the acquisition time and by the number of transmitted photons.

Samples analyzed on the SWING beamline were 20  $\mu\text{m}$  thick films annealed (-A) and melt-crystallized (-MC). For the in-situ thermal experiments, 20  $\mu\text{m}$  thick films were put in between two aluminum foils in a Linkam heating stage (THMS600). SAXS patterns were recorded every 30 s, during 200 ms, along a cooling ramp from the melt at various controlled cooling rates (2, 10 or  $50^\circ\text{C}/\text{min}$ ).

From the raw SAXS data, a background subtraction is required before analyzing the SAXS spectra  $I(q)$ . For static experiments, the background is a spectrum acquired without sample. For in-situ experiments, the background is a spectrum acquired with two aluminum foils in the Linkam heating stage. The Lorentz-corrected SAXS intensity profiles  $q^2I(q)$  were then plotted and analyzed.

For semi-crystalline polymers, the crystalline lamellae are periodically organized with the amorphous phase. The period of this organization is called long period,  $L_P$ . A correlation peak characterizing this periodic organization can be observed in  $q^2I(q)$  spectra. From the position of this peak,  $q_{max}$ , the averaged long period was determined:

$$L_P = \frac{2\pi}{q_{max}} = L_c + L_a$$

$L_c$  and  $L_a$  are the thickness of the crystalline and amorphous phases, respectively.

The calculation of the one-dimensional electron density correlation function,  $K(z)$ , is commonly used for the study of semi-crystalline polymers, in order to deduce the thicknesses of the crystalline lamellae,  $L_c$ , and their periodicity,  $L_P$  [49,50]. The linear degree of crystallinity,  $L_c/L_P$ , can be deduced, and compared to the weight crystallinity deduced from WAXS measurement [49]. This calculation was first used to analyze the SAXS data by using the XSACT software [51].

In order to separate the possible different contributions in the SAXS spectra, a peak-fitting method was also applied to the intensity profiles,  $q^2I(q)$ , by using the Fityk0.9.8 software [52]. To do so, one or two phenomenological peaks (Gaussian shape) [46–48] are introduced in addition to the conventional peak (Split Gaussian shape) associated to the crystalline lamellae periodic organization.



### 3. Results and discussion

#### 3.1. Striking influence of thermal treatments on the morphology

AFM images of Terpo65-0 with three different thermal treatments (SC, A10, MC10) are shown in Fig. 1. After spin-coating (Fig. 1a), the morphology is homogeneous and consists of very thin grains (10–15 nm width). This morphology has already been observed for P(VDF-co-TrFE) copolymers [26,27]. After annealing (Fig. 1b), the width of the grains increases (40–50 nm) with a visible periodic stratification (~15 nm). A similar periodic stacking of crystalline lamellae in annealed copolymer thin films has been recently shown by Hafner et al. [30] After recrystallization from the melt at 10 °C/min, the morphology is very different, as shown in Fig. 1c. The crystalline structures become longer and thicker and some of them have grown perpendicularly to the silicon substrate (Figs. SI-1 for AFM images at larger scale), with the so-called « edge-on » lamellar orientation. A periodic organization is still visible, with two characteristic distances: the first remains at ca. 15 nm, while the second is ca. 30–40 nm. The overall width of the lamellar stack is ca. 200 nm. This evolution of morphology after crystallization from the melt is in accordance with the existing AFM studies on P(VDF-co-TrFE) copolymer thin films [27,28].

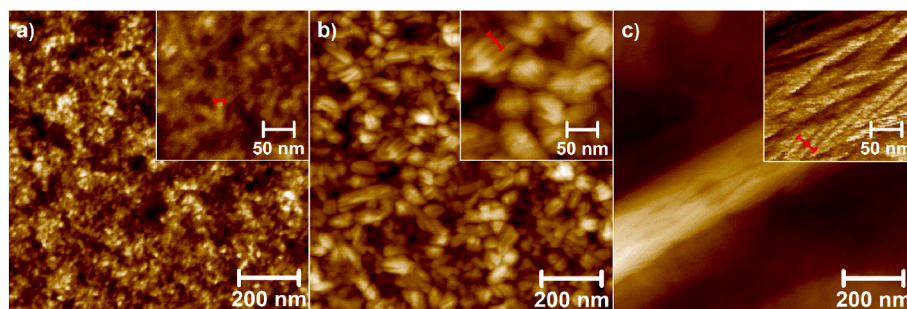
AFM analyses were able to highlight the interphase between the crystalline and amorphous phases. In Fig. 1b and c, light elongated domains are separated by thinner dark lines. This colour alternation in AFM topography images corresponds to different heights, but AFM DMTModulus images showed that a colour contrast also exists while measuring mechanical properties (Inset in Fig. 1c and Figs. SI-2a): the light domains (~15 nm width) have a higher rigidity than the dark ones. This means that the colour contrast in AFM images corresponds to the alternation of crystal (light domains) and amorphous phases (dark lines). Since the AFM tip size (5–10 nm) is comparable to the characteristic lengths that it measures, the tip cannot fully penetrate into the amorphous phase, due to size and geometry constraints. Therefore, an underestimation of the amorphous phase thickness and an overstatement of the crystalline lamellae thickness exist. These results and interpretations are in accordance with a recent study [30], which uses AFM analyses (topography and mechanical images) to determine the morphology of a thin film of P(VDF-co-TrFE) copolymer annealed above the Curie transition. Hafner et al. deduced that the semi-crystalline domains are described as rice-like domains consisting of stacks of lamellae [30]. The thickness of both crystalline lamellae and their period are given (5–8 nm and 10 nm respectively) [30]. On the other hand, the thick black lines observed on Fig. 1c could correspond to larger amorphous zones.

Fig. 2a–c shows the SAXS spectra of Terpo65-0 films prepared with the three processing conditions. The SAXS signals are very different for these three films both in shape and position. The classical method to analyze SAXS spectra of semi-crystalline polymers is to calculate the correlation function [49]. This function is then interpreted in terms of electron density distribution, associated with the crystalline lamellae

separated by the amorphous phase and organized periodically [50]. The normalized one-dimensional electron density correlation functions  $K(z)/K(0)$  were calculated from the SAXS data of the three samples and were reported in Fig. 2a'–c'. Based on the two-phase model of crystalline lamellae periodically stacked with the amorphous phase, various dimensions can be deduced. The long period  $L_p$  was deduced from the position of the first maximum of  $K(z)$  and the thickness of the crystalline lamellae  $L_c$  (or of the amorphous layer,  $L_a$ ) was measured at the intersection between the two tangents, as shown in Fig. 2a' [50].

For the as-cast film (Terpo65-0-SC), the characteristic distance associated with the position of the maximum ( $q_{max}$ ) of the  $q^2I(q)$  peak is close to 14 nm. The long period,  $L_p$ , and the crystalline lamellae thickness,  $L_c$ , deduced from  $K(z)$  are respectively 13 nm and 3 nm, leading to a linear crystallinity around 23%, which is consistent with the weight crystallinity of 20% (Tables SI-1). For Terpo65-0-A, the SAXS profile is shifted to lower  $q$ . The maximum of the SAXS signal and the position of the first maximum of  $K(z)$  are close to 30 nm, while the thickness of the crystalline lamellae is around 4.5 nm, leading to a ratio around 15%. For Terpo65-0-MC, again, the two maxima, for  $q^2I(q)$  and for  $K(z)$  are associated with a distance around 70 nm, while the thickness of the crystalline lamellae remains small, around 6 nm, which leads to a linear crystallinity around 9%. These linear crystallinities (15% and 9%), deduced from the correlation function analysis, and respectively for the annealed and melt-crystallized films, are lower than those estimated on the as-cast film (23%). However, it is well known that annealing leads to an increase in crystallinity. The influence of annealing on the crystallinity of these polymers has already been studied and an increase by a factor of 1.8 has been measured [15,18]. For these two samples, Terpo65-0-A and Terpo65-0-MC, the correlation function,  $K(z)$ , is ill-defined and spreads over a wide range of distances. Moreover, the characteristic distances, highlighted by AFM, 30–40 nm and the period of 15 nm (Fig. 1b and c) do not appear in the correlation functions. These observations show that the simple periodic two-phase model does not correctly represent the morphology of annealed and melt/crystallized films. To better analyze these SAXS profiles, and to highlight the different contributions, a peak fitting method was used. In particular, this allows us to take into account the periodicity around 15 nm, observed in all the AFM images. Although rarely used to analyze SAXS spectra, this method has already been reported in the literature [46–48].

Fig. 3a shows the spectrum for Terpo65-0-SC: the detected peak corresponds to the periodic distance of  $L_p = 14$  nm. For annealed and melted-crystallized films, the SAXS signals (Fig. 3b and c) were decomposed using the minimum number of peaks while keeping the broad and slightly asymmetrical peak, associated with the periodicity of the crystal lamellae ( $L_p$ ), deduced from Fig. 3a. For all the SAXS spectra analyzed subsequently, the lamellar peak will be represented in red, indexed with the value of  $L_p$ , the other contribution will be represented by a blue envelope, obtained by the superposition of one or two phenomenological peaks approximated by Gaussian functions (Fig. 3). For Terpo65-0-A (Fig. 3b), the additional contribution (blue envelope) to the lamellar peak is slightly asymmetric and corresponds to a distance



**Fig. 1.** AFM topography images (1  $\mu\text{m} \times 1 \mu\text{m}$ ) for a) Terpo65-0-SC, b) Terpo65-0-A10, and c) Terpo65-0-MC10. The insets are zooms corresponding to images (250 nm  $\times$  250 nm) and showing characteristic distances around 15 nm. The inset in c) is a DMTModulus image to highlight the shorter periodic distances.

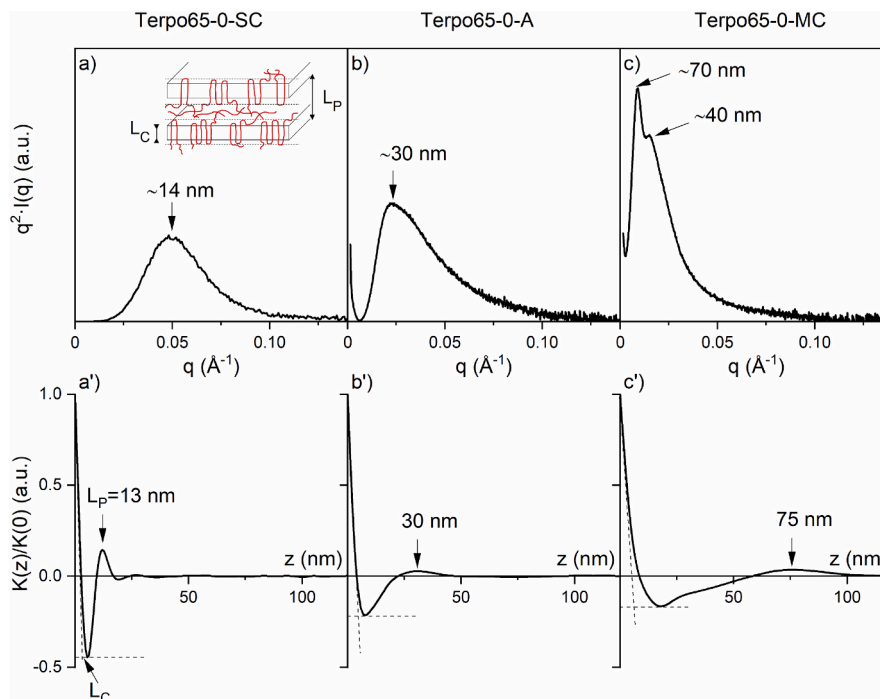


**Fig. 2.** a), b), c) SAXS spectra  $q^2 I(q)$  and a'), b'), c') normalized electron density correlation function  $K(z)/K(0)$  for a), a') Terpo65-0-SC, b), b') Terpo65-0-A, and c), c') Terpo65-0-MC. The intensity scale is the same for a), b), and c).

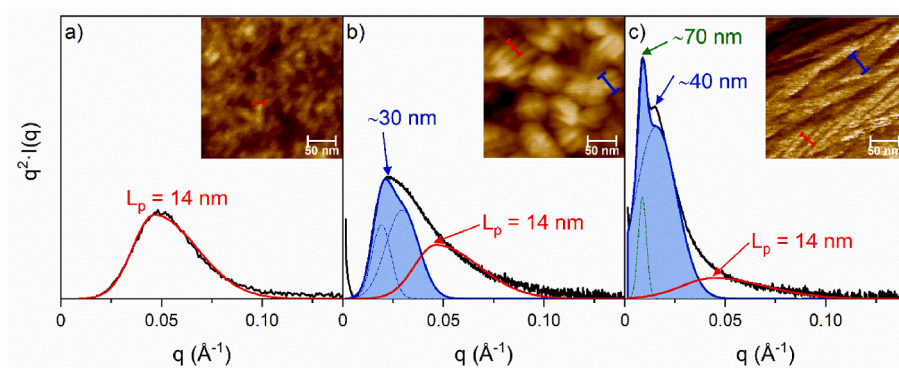


**Fig. 3.** Results of the peak-fitting method applied to a) Terpo65-0-SC, b) Terpo65-0-A, and c) Terpo65-0-MC. The insets highlight characteristic distances of 15 nm in red and around 30–40 nm in blue. The intensity scale is the same for a), b), and c). (For interpretation of the references to colour in this figure legend, the reader is referred to the Web version of this article.)

of 30 nm. Fig. 3c shows that, after crystallization from the melt (Terpo65-0-MC), the additional contribution (blue envelope) to the lamellar peak is intense and obviously composed of two peaks associated to characteristic distances of 70 and 40 nm.

AFM and SAXS measurements gave consistent results for the three different processing conditions. The 14 nm periodic distance detected by SAXS for the as-cast sample corresponds to its long period ( $L_p$ ), represented by a sketch in Fig. 2a. This SAXS signal, still present for Terpo65-0-A and Terpo65-0-MC (red peak at 14 nm), reflects the AFM observations, as highlighted by the red lines in Fig. 3b and c. Moreover, the correlation of AFM and SAXS was also possible for the 30–40 nm distance (highlighted in blue, both in the fit and in AFM inset, Fig. 3b and c), showing that lamellae were able to organize in stacks of different extension. The melting, followed by the subsequent crystallization in the high temperature phase, above the Curie transition, allows the crystalline lamellae to stack over a longer distance. The SAXS-AFM correlation is more delicate for the last distance detected in Fig. 3c: the green peak is associated with a characteristic distance of 70 nm, while the width of the

crystalline structures observed by AFM (Fig. 1c) is four times larger. This distance ca. 70 nm, has already been reported in the literature for a P (VDF-co-TrFE) melted and slowly cooled [46]. This point will be discussed later.

In the continuation of the study, this peak-fitting method will be used to highlight the various contributions of the SAXS spectra.

At this step of the study, one can wonder if the comparison of the evolutions observed, on the one hand, at the surface of thin films by AFM and, on the other hand, in the bulk of thick film by SAXS is relevant. To be convinced, both the surface and the cross-section of the thick films were observed by scanning electron microscopy (SEM). The observations carried out on the thick films effectively show the same type of morphology as those observed by AFM on thin films, for annealed and melt-crystallized films. Small rice-like domains around 30 nm are observed for the annealed film (Figs. SI-3a and 3a') and long multi-sheets micrometric domains with a thickness around few 200–300 nm are observed after crystallization from the melt (Figs. SI-3b and 3b'). It therefore seems quite relevant to correlate the evolutions observed on

the one hand by AFM on thin films and on the other hand by SAXS on thick films, when the same variable parameter evolves. For example, this parameter can be the temperature or the chemical composition.

### 3.2. Effect of annealing on the morphology

#### 3.2.1. Annealing of the P(VDF-co-TrFE) copolymer

The P(VDF-co-TrFE) copolymers have a specific behavior during annealing, since this thermal treatment is performed above the Curie transition (in the paraelectric phase). At this temperature, some polymer chains containing conformational defects can crystallize. These chains were not able to crystallize at room temperature, after the evaporation of the solvent [15]. The change of morphology observed both by AFM and SAXS, after annealing, reflects the crystallization of the defective ferroelectric phase. In order to better understand this evolution, in-situ AFM and SAXS analyses were performed on Terpo65-0-SC during a heating ramp from room temperature to the annealing temperature. The AFM images are shown in Fig. 4a–e.

At 60 °C (Fig. 4a), the morphology is roughly similar to that of the as-cast sample at room temperature, shown in Fig. 1a. At 90 °C (Fig. 4b), the polymer undergoes the Curie transition: the small light areas, interpreted as semi-crystalline domains, become thicker and their shape seems better defined. A further increase in temperature, up to the annealing temperature of 130 °C, leads to progressive thickening of these semi-crystalline domains (Fig. 4c and d). At 130 °C, the morphology seems more elaborated, with a periodic stratification visible within some domains. After 1 h of annealing, the morphology remains unchanged (Fig. 4e) and after cooling down to room temperature no important change is observed.

SAXS spectra, acquired on the Nano-inXider during 60 s at each selected temperature, are reported in Fig. 4a'–e'. During heating, the spectra show an evolution of both intensity and shape. First, at 60 °C, only the intensity increases (30% compared to 20 °C). This temperature is just before the Curie transition for Terpo65-0-SC. Starting from the SAXS spectrum at 90 °C (Fig. 4b'), the position and the shape of the signal evolve until reaching a spectrum which is similar to the one shown in Fig. 2b. The same peak-fitting procedure was used to visualize various contributions in the SAXS spectra at each temperature. The slightly asymmetric peak associated to the long period is kept (red peak); its intensity and position are adjusting parameters. Another contribution (blue envelope) appears at lower  $q$  values ( $\sim 0.025 \text{ \AA}^{-1}$ ) when the temperature increases. As shown in Fig. 4a'–e', this additional signal changes with increasing temperature, from thin and symmetrical to broad and asymmetrical. At the same time, its characteristic distance increases from 18 to 35 nm. This evolution can be interpreted by considering the structural evolution of the polymer from the solvent-cast

state to the annealed one, i.e. by considering the creation of the defective ferroelectric (DFE) crystal phase. First, the significant decrease of the intensity above the Curie transition is interpreted considering the change of the crystal density with temperature, mostly by the disappearance of the dense FE phase [15]. At 90 °C, the Curie transition occurs: part of the ferroelectric phase has already transited towards the paraelectric phase and, at the same time, small segments of polymer chains crystallize. These chains crystallize in the PE phase and they will constitute the DFE phase after cooling down to room temperature [16]. The crystallization of these chains is reflected by the appearance of the extra peak, associated with a distance of ca. 18 nm. When the temperature increases, this peak shifts towards a distance of ca. 35 nm while widening. After cooling back to room temperature, the SAXS signal does not return to its original position and shape, it only shifts slightly towards larger  $q$  values and its asymmetric shape remains unchanged, similar to that reported in Fig. 3b.

Without giving a strict meaning to the distances deduced from the peak-fitting method, an overall interpretation of the evolution of the spectra can be discussed in connection with that of the AFM images. First, the initial lamellae periodicity ( $L_p = 14 \text{ nm}$ ) seems preserved, it is visible on the AFM image and in the SAXS spectra (Fig. 3b), while new characteristic distances around 30 nm appear and are linked to the crystallization of the DFE phase. The crystallization of this DFE phase during the annealing above the Curie transition is associated with the growth of the stacked crystalline domains observed by AFM (Figs. 1b, 3b and 4).

Several publications have reported the irreversible evolution of the SAXS signal observed on P(VDF-co-TrFE), after annealing [23] or after a first heating above the Curie transition [15,31,32,36]. Most of the authors assumed that the shift of this SAXS signal towards lower  $q$  was associated with an increase of the long period,  $L_p$ , due to the transition towards the high temperature phase [23,32]. By combining AFM and SAXS studies during heating, it can be concluded that  $L_p$  is not significantly affected, but annealing at high temperature in the PE phase enables the growth of semi-crystalline domains, thanks to the crystallization of the defective phase. These semi-crystalline domains are responsible of the broad peak at low  $q$  in the SAXS spectra (ca. 30 nm). This interpretation concurs with the hypothesis put forward by Bourgaux et al. [31] and Tashiro et al. [23] to explain the substantial SAXS evolution by « another superstructure » or « the formation of higher-order structure ».

#### 3.2.2. Annealing of terpolymers: effect of the composition

Topography images for all as-cast samples showed very similar results to those showed in Fig. 1a for Terpo65-0-SC. For this reason, they will not be detailed in this section.

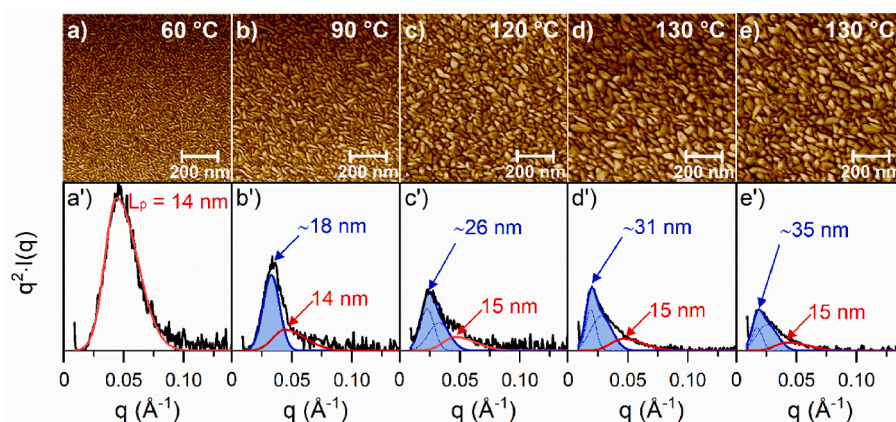


**Fig. 4.** In-situ AFM phase images ( $1 \mu\text{m} \times 1 \mu\text{m}$ ) and SAXS spectra for Terpo65-0-SC during a heating ramp. a), a') 60 °C, b), b') 90 °C, c), c') 120 °C, d), d') 130 °C, and e), e') at 130 °C, after 1 h. The intensity scale is the same for a'), b'), c'), d'), and e').



AFM images for annealed thin films with increasing CTFE amounts are presented in Fig. 5. For Terpo65-0-A10, the observed morphology has already been discussed: the average width of the crystalline domains is ca. 40–50 nm, while their average length is ca. 85 nm. Their form factor, defined as the ratio length/width, is around 1.7. Each domain is made of 3–4 stacked lamellae, which have 15 nm period and are clearly visible in the AFM image (Fig. 5a). When the CTFE amount increases, the form factor of the crystalline domains progressively increases until a value of 4 for Terpo68-10.3-A10. Since the domains become thinner and thinner for higher CTFE content (25 nm), as shown in Fig. 5d and e, the stacking of lamellae is less extended (down to two lamellae). Moreover, the dark lines which separate two lamellae are less and less visible when the CTFE amount increases (Figs. SI–2). The evolution of the size of semi-crystalline domains, decreasing when the CTFE content increases, could also be linked to an increase in the nucleation density with the CTFE content. It is difficult to conclude on this point, many parameters being able to intervene, such as the specific interactions with the solvent which could evolve with the chemical composition of the chains.

SAXS analyses were also performed on samples with the same compositions and thermal treatments, but with a thickness of 20  $\mu\text{m}$ . A thinning of the semi-crystalline domains was also confirmed by SEM observations (thickness around 20 nm) on the surface and in the bulk of the Terpo67-8.3-A thick film (Figs. SI–4a and 4a'). Even if the SAXS spectra on as-cast films are not shown here, they are nonetheless briefly discussed to complete the framework for the annealed morphology. The long period,  $L_p$ , increases from 14 nm to 19 nm when the CTFE amount increases from 0 to 10 %CTFE (see Tables SI–1). This slight evolution can be interpreted as a thickening of the crystalline lamellae when the CTFE amount increases. These CTFE units, randomly distributed along the polymer chains, are incorporated both into the crystalline lamellae and in the amorphous layer. These bulky repetitive units stiffens the chains, and disfavour their folding, during crystallization, at the edge of the crystalline lamellae [53].

In order to deduce characteristic dimensions from the SAXS spectra of the annealed terpolymers (Fig. 6), the phenomenological peak-fitting method already described was used. To perform their peak-fitting, the signal of the solvent-cast long period for each composition (same position and shape as in Tables SI–1, coloured in red in Fig. 6) was used. This choice is justified because the samples remained below the melting temperature during the thermal treatment and the initial lamellar periodicity seems preserved, according to Figs. 1b and 5.

For Terpo65-0-A (Fig. 6a), the SAXS signal has already been discussed in paragraph 3.1. Apart from the as-cast long period contribution (red peak), the added asymmetric contribution is fitted with two peaks (one blue and one grey), which have similar intensities. For Terpo66-4.7-A and Terpo67-6.4-A (Fig. 6b and c), the shape of the added contribution, which becomes more symmetric, is still fitted with two additional peaks. In the blue envelope, the blue peak attributed to the highest characteristic distance (ca. 33 nm) is increasingly intense compared to the other grey peak, when the amount of CTFE increases. For Terpo67-8.3-A and Terpo68-10.3-A, the spectra are essentially fitted with the single blue peak in addition to the red lamellar peak (Fig. 6d and e). The intensity of the second grey peak decreases significantly, while its position shifts towards higher  $q$  values. This evolution which reflects the fact that the SAXS signal becomes more and more symmetrical, could be associated with a more homogeneous size distribution of the semi-crystalline domains. The quality of the peak-fitting was represented in Figs. SI–5 by the superposition of the experimental curve and the summed curve resulting from the fit, for all the compositions.

For the P(VDF-co-TrFE) copolymer and the P(VDF-*ter*-TrFE-*ter*-CTFE) terpolymer with 4.7 %CTFE, crystalline domains consist of ferroelectric (FE) and defective ferroelectric (DFE) phases, with the respective DFE/FE ratio of 50/50 and 60/40, while for terpolymers with high amounts of CTFE (>6 %CTFE) there is almost only the relaxor ferroelectric (RFE) phase [18]. These different crystalline (FE, DFE, RFE) and amorphous (Am) phases introduce different interphases: FE/Am, DFE/Am, and FE/DFE for the copolymers and terpolymers with low amount of CTFE, or RFE/Am for the terpolymers with a high amount of CTFE [16]. These interphases can be responsible for different contrasts at the origin of SAXS signals. It can be observed that samples containing both the FE and DFE phases lead to broader and asymmetric SAXS spectra, while the presence of the single RFE phase leads to narrower and symmetric spectra (Fig. 6). The presence of the FE and DFE phases also leads to the crystallization of objects with a smaller form factor (1.7), whereas the sole presence of the RFE phase leads to narrower and elongated domains (Fig. 5). At 130 °C, the crystalline phase of Terpo65-0 only consists of the PE phase, which means that only the PE/Am contrast can exist at this temperature. Yet, the SAXS spectra observed in Fig. 4 are already asymmetric. This observed asymmetry is therefore not linked to several contrasts appearing at various characteristic distances. It can thus be concluded that the blue peaks observed in the SAXS signals are related to the shape of the semi-crystalline domains observed on the AFM images.

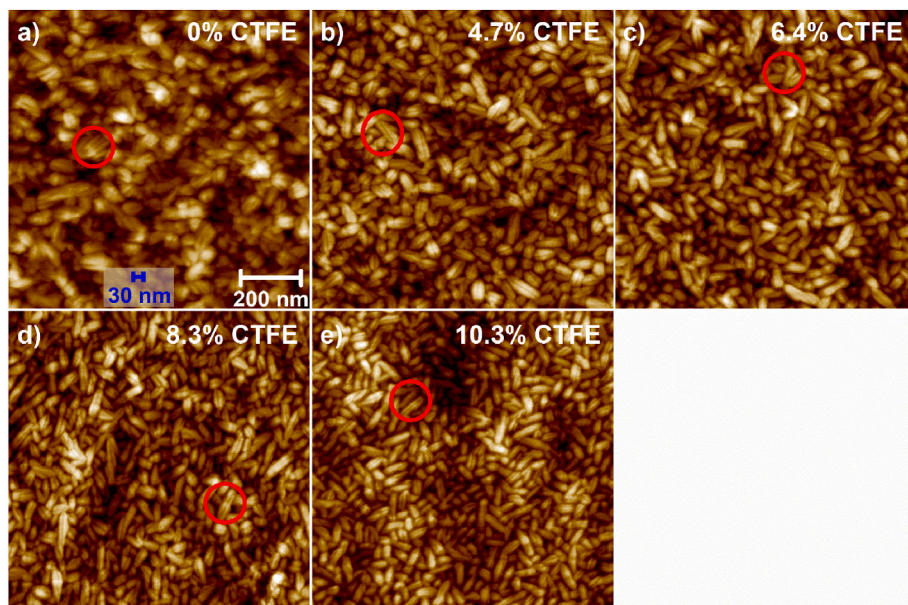
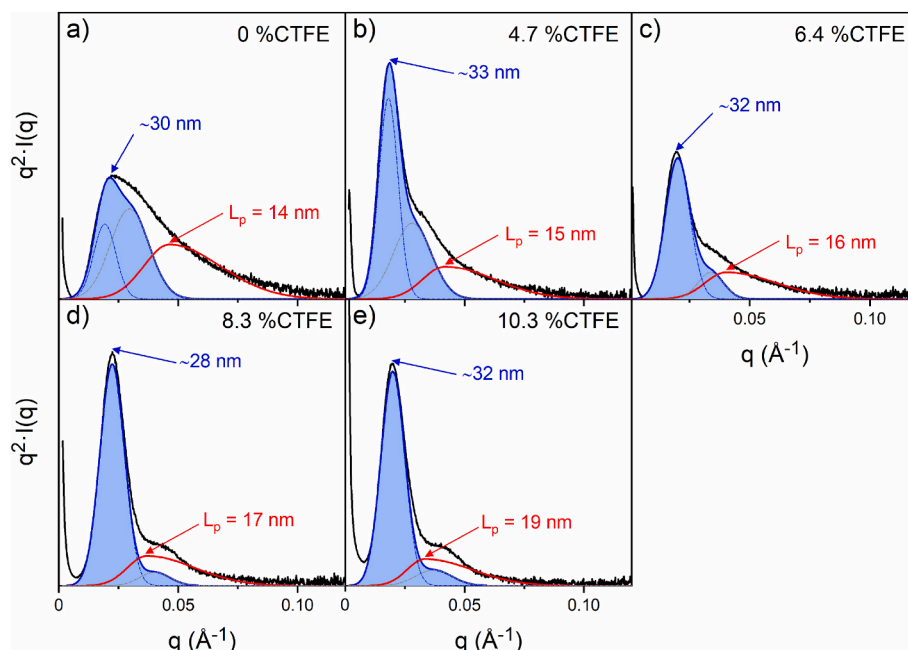


Fig. 5. AFM topography images ( $1\ \mu\text{m} \times 1\ \mu\text{m}$ ) of annealed samples with different compositions. a) Terpo65-0-A10, b) Terpo66-4.7-A10, c) Terpo67-6.4-A10, d) Terpo67-8.3-A10, and e) Terpo68-10.3-A10. Red circles highlight elongated clear domains separated by thinner dark lines, discussed in the text and associated respectively with crystalline and amorphous phases. (For interpretation of the references to colour in this figure legend, the reader is referred to the Web version of this article.)



**Fig. 6.** SAXS spectra for a) Terpo65-0-A, b) Terpo66-4.7-A, c) Terpo67-6.4-A, d) Terpo67-8.3-A, and e) Terpo68-10.3-A. Two main contributions are highlighted: the long period contribution in red and the blue envelope, formed by the two blue and grey peaks, and discussed in the text. The intensity scale is the same for a), b), c), d), and e). (For interpretation of the references to colour in this figure legend, the reader is referred to the Web version of this article.)

We can conclude that the contribution represented by the blue envelope (Fig. 6), which is more and more symmetric when the amount of CTFE increases, is well correlated with the size and shape distribution of the domains observed on the AFM images (Fig. 5). Indeed, the image associated to the Terpo68-10.3-A10 (Fig. 5e) shows a more homogeneous morphology distribution than that observed for the Terpo65-0-A10 (Fig. 5a).

For all compositions, the red peaks at ca. 15 nm in Fig. 6, associated with the long period and created in solvent cast films, may be associated with the periodicity of the thin black lines observed in the AFM images in Fig. 5, although this distance may increase following the crystallization of the DFE phase. It can thus be concluded that the SAXS spectra

recorded on thick 20  $\mu\text{m}$  films are consistent with the AFM images observed on thin 100 nm films. The SAXS spectra reflect both the shape of the semi-crystalline domains and the periodicity of the crystalline lamellae. From these AFM and SAXS studies, it can be concluded that the semi-crystalline domains, formed after annealing above the Curie transition, depend on the amount of CTFE. For a low amount of CTFE, the semi-crystalline domains grow by stacking of periodic crystalline lamellae, whereas for a large amount of CTFE, the crystalline lamellae extend laterally to form thin and elongated semi-crystalline domains.

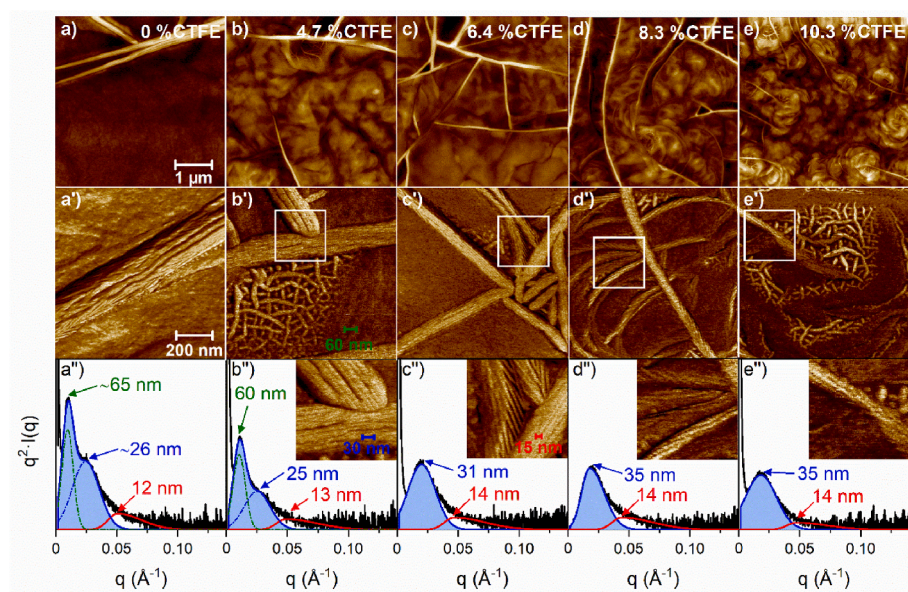


**Fig. 7.** AFM topography images ( $5 \mu\text{m} \times 5 \mu\text{m}$ ), mechanical images ( $1 \mu\text{m} \times 1 \mu\text{m}$ ), and SAXS spectra (Synchrotron Soleil) for a), a'), a'') Terpo65-0-MC10, b), b'), b'') Terpo66-4.7-MC10, c), c'), c'') Terpo67-6.4-MC10, d), d'), d'') Terpo67-8.3-MC10, and e), e'), e'') Terpo68-10.3-MC10. Insets in b'' to e'') correspond to the enlargement by a factor 2 of the white square drawn ( $250 \text{ nm} \times 250 \text{ nm}$ ) in images b') to e'). The intensity scale is the same for a'), b'), c'), d'), and e').



### 3.3. Morphologies of melt-crystallized terpolymers

After crystallization from the melt, very large and rectilinear semi-crystalline domains were observed for the Terpo65-0-MC copolymer, as shown in Fig. 1c. Interesting changes in these morphologies were observed when the composition of the terpolymer changes, i.e. the CTFE content, and when the cooling rate varies. The influence of each of these two parameters will be discussed.

#### 3.3.1. Melt-crystallized morphologies: impact of the terpolymer composition

To better visualize the morphologies observed after crystallization from the melt, Fig. 7 combines AFM topography and DMTModulus images (Fig. 7a–e and 7a'–e', respectively) and SAXS spectra (Fig. 7a''–e'') for samples crystallized from the melt at 10 °C/min.

As already mentioned for Terpo65-0-MC10, the crystallization from the melt induces the formation of very long and wide semi-crystalline domains (Fig. 7a). The micrometric size of these domains is better appreciated using optical microscopy (Figs. SI–6). These domains correspond to lamellar stacks (Fig. 7a') that have partially grown perpendicularly to the substrate («edge-on») and partially in parallel to the substrate («flat-on») (Fig. 7a). With increasing amount of CTFE, these straight, thick and long domains evolve. This evolution appears clearly both on the observations by AFM (Fig. 7) and by optical microscopy (Figs. SI–6). On the latter, a very significant evolution of the nucleation density appears clearly. Increasing the CTFE content in the terpolymer would induce a significant increase in crystallization seeds density. The semi-crystalline domains become less and less straight and thick, their lateral extension decreases until reaching a size lower than 1  $\mu\text{m}$  (Fig. 7).

For a large amount of CTFE, these sub-micrometric domains seem to pile up like plates (Fig. 7d–d') or to combine into petals in flower-like structures (Fig. 7e–e'). For all the compositions, thin periodic dark lines ( $\sim 15$  nm) are still visible on the AFM DMTModulus images (Inset in Fig. 7b'–e''). As previously discussed, they are attributed to amorphous and crystalline lamellae. These thin dark lines are organized in rectilinear periodic domains (15 nm period) separated by thick dark lines spaced about 30–40 nm apart, for the Terpo65-0-MC10 and Terpo66-4.7-MC10 (Fig. 7a'–b'). For higher amount of CTFE, the thick dark lines disappeared, while the thin dark lines seem to be organized periodically in curved or twisted domains having a thickness around 30–50 nm (Fig. 7c'–e'). Once again, complementary SEM observations were made on the Terpo67-8.3-MC thick film on the surface and in the bulk (Figs. SI–4b and 4b'). The similarity of the AFM image of Fig. 7d' and SEM image of Figs. SI–4b is really striking, with domain thickness around 40 nm. The SAXS spectra (Fig. 7a''–e''), acquired on thick films, show a wide and more or less asymmetric peak for all the compositions, while an additional peak at small  $q$  values exists only for low %CTFE samples. Once again, a peak-fitting method was applied in order to separate contributions using a minimum number of peaks. At high  $q$ , a small asymmetric peak is positioned and associated to the amorphous and crystalline periodicity, and one or two phenomenological peaks are added in the lower  $q$  range to reproduce the SAXS profiles. The blue envelope is asymmetric and fitted with two peaks, for the lower amounts of CTFE. The peak at lower  $q$  (green peaks in Fig. 7a''–b'') always appears at the same time as the large micrometric semi-crystalline domains (Fig. 7 and SI-3). However, the distance associated with this peak, ca. 60 nm, is not linked to a characteristic distance measured on the AFM images. At high  $q$ , it seems obvious to associate the red peak around 12–14 nm with the periodic organization of the crystalline and amorphous lamellae. As with the solvent-cast samples, this long period (red peak) would increase slightly with the amount of CTFE, while the blue peak around 30–35 nm would correspond to a characteristic size inside which the periodic crystalline lamellae are organized. It corresponds to the distance between thick dark lines, for the Terpo65-0-MC10 and Terpo66-4.7-MC10 (Fig. 7a'–b'), or to the thickness of the semi-crystalline domains for higher amounts of CTFE (Fig. 7c'–e').

In the next section, the effect of the cooling rate on the morphologies during crystallization from the molten state, is studied for Terpo67-8.3-MC.

#### 3.3.2. Melt-crystallized morphologies: impact of the cooling rate from the molten state

In order to better understand these structures, different cooling rates were chosen, ranging from 1 to 100 °C/min. AFM topography images are shown in Fig. 8 for Terpo67-8.3-MC, and optical microscope images are reported in Figs. SI–7. Fig. 8a and b shows that at very low cooling rates, lamellar stacks are straight, with a large stacking extension (150 nm) and lateral extension (few micrometers). Starting from 10 °C/min (Fig. 8c), both thickness of the straight stacking and lateral extensions start to decrease.

The predominant morphology at high cooling rates consists of small petal-shaped crystalline domains, with a short lateral extension (Fig. 8f) and capable of stacking in large numbers, like flowers. When the cooling rate decreases (Fig. 8c and d), their lateral extension increases and a stacking is still visible. At 10 °C/min and 20 °C/min the semi-crystalline domains appear as stacked flat discs. At very low cooling rates (Fig. 8a and b), their lateral extension becomes very high and the stacking of some crystalline lamellae is perfected, and enabling straight « edge-on » and « flat-on » semi-crystalline domains. For these two slow cooling rates, the thick dark lines discussed earlier (Fig. 8a and b) are clearly visible.

The effect of the cooling rate from the molten state on the morphology of P(VDF-co-TrFE) thin films (50 and 100 nm) was previously studied by AFM by Lee et al. [27], who showed that the crystallization from the melt induces a preferential flat-on orientation. Along with this majority orientation, a very fast cooling generates minority long and thin edge-on lamellar stacks, while a cooling at 2 °C/min induces the formation of minority shorter and larger edge-on stacks [27]. The results reported in Figs. 7 and 8 show the same trend, which can be extended to P(VDF-ter-TrFE-ter-CTFE) terpolymers. For low cooling rates (and/or low amounts of CTFE), the rectilinear semi-crystalline domains are predominant: they can present two particular orientations, perpendicular or parallel to the substrate for the « flat-on » or « edge-on » configurations, respectively. As a tilt of the thin lamellae was observed (Figs. 1c and 7), it cannot be assessed that the chains are perpendicular or parallel to the substrate for the « flat-on » or the « edge-on » orientations, respectively, but chains have a well-defined overall orientation. However, for high cooling rates (and/or high amounts of CTFE), the stacked-plate or flower-like morphologies, which are predominant, have no longer a specific orientation. Thus, in that case, the polymer chains will not have a specific orientation with respect to the substrate.

AFM analyses for all compositions and for all cooling rates were done and similar trends were found. As observed in Fig. 8, the number of « edge-on » domains decreases significantly with increasing CTFE amount and/or cooling rate, but a few remain. The average width of these « edge-on » lamellar stacks was measured and plotted against cooling rate, as shown in Fig. 9.

For all the compositions, the average width of the « edge-on » semi-crystalline structures decreases while the cooling rate increases. This decrease is very pronounced for Terpo65-0-MC and much less important for Terpo68-10.3-MC. For a same cooling rate, the average stacking thickness of lamellar stacks decreases while %CTFE increases: the higher the CTFE amount, the thinner the domains.

Increasing the cooling rate or the amount of CTFE influences the crystallization in the same way. If the cooling rate increases, the crystallization temperature decreases, the nucleation density increases, and the mobility of the chains, at the crystallization temperature, decreases. If the CTFE amount increases, a stiffening of the polymer chains is expected and an increase in the number of crystallization seeds is observed. In both cases, due to the increase in the nucleation density, the number of semi-crystalline domains increases while their lateral

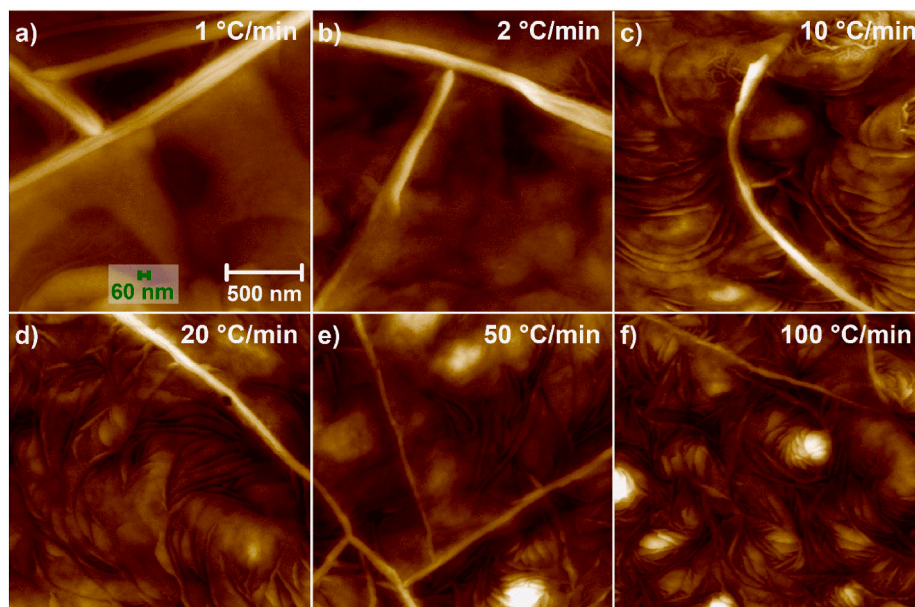


**Fig. 8.** AFM topography images ( $2\ \mu\text{m} \times 2\ \mu\text{m}$ ) for Terpo67-8.3-MC after crystallization from the melt at a)  $1\ ^\circ\text{C}/\text{min}$ , b)  $2\ ^\circ\text{C}/\text{min}$ , c)  $10\ ^\circ\text{C}/\text{min}$ , d)  $20\ ^\circ\text{C}/\text{min}$ , e)  $50\ ^\circ\text{C}/\text{min}$ , and f)  $100\ ^\circ\text{C}/\text{min}$ .

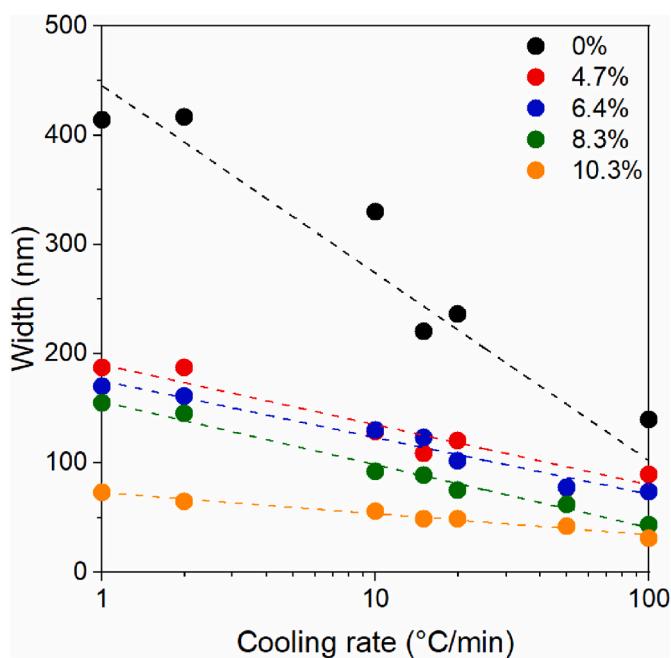


**Fig. 9.** Average width of the observed « edge-on » semi-crystalline structures vs cooling rate for 0–10.3 %CTFE samples.

extension decreases.

For controlled cooling rate ramps, the effective cooling rates are not the same inside the 100 nm films (AFM observations) and inside the 20  $\mu\text{m}$  films (SAXS acquisition), but, qualitatively, the evolution of AFM images can be compared to that of SAXS spectra when the cooling rate increases. In-situ SAXS experiments were performed using synchrotron radiation, during the crystallization of Terpo67–8.3 from the melt at various cooling rates (2, 10, and  $50\ ^\circ\text{C}/\text{min}$ ). The 3D representations are given in SI (Figs. SI–8), while the spectra recorded at  $25\ ^\circ\text{C}$  after the three cooling ramps are reported in Fig. 10.

Again, only the spectrum obtained after slow cooling shows a peak at small  $q$  (green peak in Fig. 10a), associated with a distance of 80 nm.

This peak appears concomitantly with the large rectilinear domains observed in Fig. 8a and b and Figs. SI–7, but, once again, the distance associated with this peak is not easily interpreted with the AFM images. The other (red and blue) peaks observed for all cooling rates are associated respectively with the periodic stacking of crystalline lamellae ( $L_p$ ) and with the organization of these lamellae packs into plates or petals. The smaller petals would perhaps be better defined or organized (high number of petals in stacks) leading to the thinner blue peak at high cooling rate.

### 3.4. Discussion

Thanks to these SAXS and AFM experiments, our vision of the crystallization and of the morphologies developed in these unconventional fluorinated copolymers can now be discussed. Indeed, these copolymers consist of isomorphous monomers, the spherulitic morphology of their parent PVDF has never been observed, and finally, they exhibit a crystal-crystal transition with temperature. These particularities are at the origin of the very different morphologies reported in the literature, for different compositions and/or processing conditions.

After the solvent evaporation, small crystalline lamellae ( $L_p \sim 15\ \text{nm}$ ) were observed, by SAXS and AFM, and no superstructure was evidenced.

The annealing step, necessary to optimize both the electroactive properties and the temperature stability of these copolymers, takes place above the crystal-crystal (Curie or pseudo-Curie) transition. The crystallization that takes place in this high temperature phase (PE) irreversibly modifies the morphology. The obtained morphology depends on the amount of CTFE. For low CTFE content, semi-crystalline domains are observed, with a fairly isotropic grain shape with a length close to 85 nm (shape factor  $<2$ ). These grains consist of a stacking of crystalline lamellae ( $L_p \sim 15\ \text{nm}$ ). For high CTFE contents ( $\sim 8$ – $10\ \text{mol}\%$ ), these semi-crystalline domains are elongated, with a shape factor greater than 4 and a width close to 25–30 nm. Periodic crystalline lamellae ( $L_p \sim 15\ \text{nm}$ ) are always observed, oriented according to the length of the objects. Therefore, the crystallization and the growth of these semi-crystalline objects during annealing do not occur in the same direction for low and high CTFE contents.

After crystallization from the melt at controlled cooling rates, the observed semi-crystalline domains are always made of crystalline

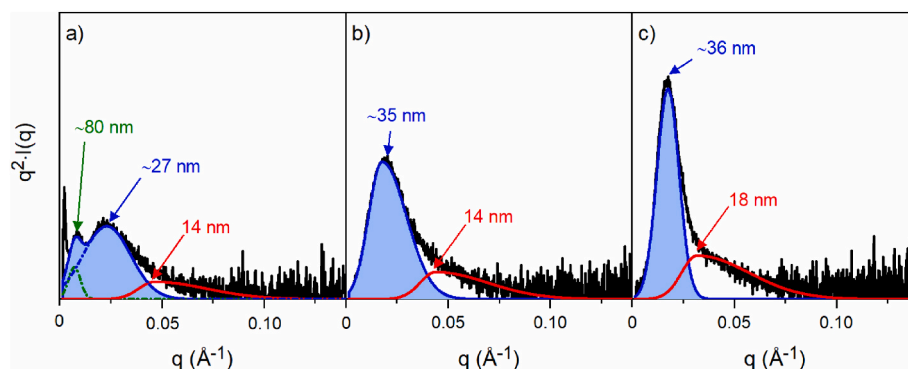


**Fig. 10.** Synchrotron Soleil SAXS spectra for a) Terpo67-8.3-MC2, b) Terpo67-8.3-MC10, and c) Terpo67-8.3-MC50. The intensity scale is the same for a), b), and c).

lamellae periodically organized with amorphous phase ( $L_p \sim 15$  nm). However, the shape of these domains strongly depends on both the CTFE amount and the cooling rate. These two parameters have the same influence on the morphologies, induced by a significant change of the nucleation density. At low CTFE content and/or at low cooling rate, the semi-crystalline domains of rectilinear shape are very long ( $>4\text{--}5\text{ }\mu\text{m}$ ) and thick ( $>100$  nm). Inside these domains, the crystalline lamellae ( $L_p \sim 15$  nm) form laterally extended sheets ( $>\mu\text{m}$ ) with a thickness around 30–50 nm (Fig. 7a-a', 7b-b' and Fig. 8a and b). The latter are superimposed to reach the total thickness ( $>100$  nm) of the domains. These large domains can easily orient on the substrate in an « edge-on » or « flat-on » configuration. For high amount of CTFE and/or high cooling rates, the lateral extension of the semi-crystalline domains decreases below the micrometer, while their thickness decreases to 30–40 nm (Fig. 7c-c', 7d-d', 7e-e' and Fig. 8c–f). These 30–40 nm thick sheets are no longer straight, they can be stacked as a pile of disorganized plates or petals in a flower-like structures, without well-defined orientation. Within these sheets, the small crystalline lamellae ( $L_p \sim 15$  nm) are always observed, more or less tilted.

Thus, after evaporation of the solvent, followed by annealing in the high temperature phase, the morphologies observed by microscopy are different from the morphologies observed after crystallization from the melt in the high temperature phase. Yet, the characteristic dimensions measured on these various AFM images are quite similar. Indeed, crystal/amorphous periods are always measured, of the order of 15 nm (distance between thin black lines in Figs. 1, Figs. 5 and 7) and domain thicknesses of the order of 30–40 nm (Figs. 3, Figure 5 and Fig. 7c–f) are frequently observed. Moreover, SAXS spectra obtained on the films annealed and melt-crystallized during cooling at high cooling rates appear similar (Figs. 5 and 9). The phenomenological peaks (blue envelope) added to the signal of the crystalline lamellae are always associated with a distance of the order of 30–40 nm. Only the spectra resulting from a slow cooling rate present an additional peak around 60–70 nm, which is not identified on the AFM images but appears systematically in concomitance with the large rectilinear domains. It can be concluded that these polymers crystallize with periodically organized lamellae, alternated to amorphous inter-lamellar layers with a long period,  $L_p$ , which around 14–18 nm depending on the CTFE content. These crystalline and amorphous lamellae are the constituting elements of semi-crystalline objects, which vary in size and shape depending on the process used, whether annealed from solvent-cast or crystallized from the melt.

Some observations by AFM microscopy exist in the literature. In particular, the morphology after annealing was finely studied by Hafner et al., the same rice-like semi-crystalline domains were observed with the identification of the crystalline lamellae separated by the amorphous phase [30]. A lamellar period of about 10 nm was measured on a P(VDF-co-TrFE) with a VDF/(VDF + TrFE) ratio of 70. Contrariwise, this periodicity of the crystalline lamellae has never been observed after crystallization from the molten state. Indeed, Lee et al. [27] and Guo

et al. [28] both have only considered that the objects they observe have dimensions compatible with periodic distances around 10–15 nm reported in the literature. To our knowledge, we are therefore the first to observe these periodic crystalline lamellae (15 nm) in melt-crystallized films.

On a P(VDF-co-TrFE) copolymer with a VDF/(VDF + TrFE) ratio of 86, slowly crystallized from the melt, SEM observations coupled to SAXS experiments have been reported [47]. At room temperature, after crystallization, two peaks were found in the SAXS spectra. These peaks are associated to distances of 74 nm and 13 nm which are interpreted as the coexistence of thick and thin lamellae stacks, the thick ones being observed by SEM. This publication would therefore confirm the existence of the peak around 70 nm that we observed after crystallization from the melt during a ramp at low cooling rate, as well as the existence of a periodic distance of ca. 13 nm (Figs. 7 and 10).

In the case of semi-crystalline polymers, SAXS spectra showing double peaks have been reported for polyethylene (PE) [47], polyoxymethylene (POM) [54], poly(aryl ether ether ketone) (PEEK) [55], and P(VDF-co-TrFE) [46]. The interpretation of these two peaks, which will be noted L1 and L2, is discussed in these various publications. For example, for P(VDF-co-TrFE), L1 and L2 distances, measured at around 70 and 13 nm, are attributed to the thickness of lamellae stacks observed by SEM. L1 correspond to a bundle size, while L2 is the crystalline lamellae periodicity [46]. In the case of PEEK, two thicknesses of crystalline lamellae, thin ones intercalated between thicker ones, are considered to explain both the temperature evolution of the long period and the double melting peak [55]. In the cases of POM [54] and PE [47], the L1 distance is twice the L2 distance, as in the case of our study. Several hypotheses are put forward by the authors. The simplest one assesses that the peak associated with L2 corresponds to the second order. In both publications [47,54], this hypothesis was eliminated considering the different temperature evolution of the two peaks. In our case, the attribution to the second order can also be eliminated, since the periodicity associated to the smaller distance L2 (15 nm) is always observed on our AFM images, it corresponds therefore to a real periodicity and not to a second order. L1 and L2 can also be associated with two different stacks of crystalline lamellae which coexist, with or without lamellae insertion. For PE and POM, studies are conducted during crystallization from the molten state. For PE, during isothermal crystallization at high temperature, lamellae included in the larger long period crystallize first with a period L1 around 80 nm, then a second generation of crystalline lamellae is created in between the first one, creating the second periodicity L2 around 40 nm. Depending on the studied PE, when the crystallization process is complete, either the two periodicities coexist or only the small one exists [47]. In the case of POM, during a non-isothermal crystallization the large periodicity ( $L1 = 14$  nm) appears at higher temperature, then the second ( $L2 = 7$  nm) appears by insertion of thin crystalline lamellae in between the main layers. At room temperature, the two periodicities, L1 and L2, coexist [54].

In our case, the coexistence of two periodicities is consistent with the



AFM observations. Indeed, the thick black lines, observed after crystallization during a slow cooling ramp (Fig. 7a'-b') and spaced by 30–40 nm could be associated with the high periodicity lamellae stacks in which the thin lamellae, associated with the periodicity of 15 nm, crystallized. At room temperature the two periodic stacks would coexist. These two periodicities would be associated with crystalline lamellae of fairly similar thicknesses; indeed, a single melting peak is observed. Only a slight evolution of the melting temperature was observed for the two thermal treatments, (Figs. SI–9). The melting temperatures measured for Terpo65-0-A and Terpo65-0-MC are 150 °C and 153 °C, respectively, showing that the thickness of the crystalline lamellae is the same after annealing and after melt-crystallization. For high cooling rates, this periodicity (30–40 nm) could be the stacking periodicity of plates or petals in stacked-plate or flower-like morphologies, respectively (Fig. 8c–f).

Compared to the melt-crystallized morphologies, those observed after annealing are very small. Indeed, annealing was performed on solvent-cast films which exhibit very thin morphologies. The growth of the semi-crystalline domains, during annealing, takes place in the volume available between these pre-existing lamellae. One can wonder about the meaning of the characteristic distance of 30–40 nm in the annealed films. During annealing at  $T_m - 15$  °C, some chain segments crystallize in the paraelectric phase, but the crystallization is unlikely to occur with a period of 30–40 nm, around the pre-existing lamellae. Doubling of lamellae during annealing have already been observed, but with annealing temperatures very close to the melting temperature, which allows a mechanism of partial melting and rearrangement, for example observed in polyethylene [56]. In our case, the annealing temperature is far from the melting one, and the second characteristic distance increases progressively during heating (Fig. 4) from 20 nm at 90 °C to 30–40 nm after 1 h annealing at 130 °C. This progressive evolution would rather correspond to an increase in size of the semi-crystalline domains and not to a double periodicity as observed in the film crystallized from the molten state.

#### 4. Conclusion

In this study, it has been shown that the combination of AFM and SAXS analyses can be very rich and informative to understand the crystallization of fluorinated copolymers and terpolymers. In this type of combined AFM and SAXS study, it is not necessary to seek a perfect agreement of the distances, measured by the two methods, because the analyzed samples (thicknesses) as well as the probed volumes are different. On the other hand, it is possible to follow the influence of a same variable parameter (chemical composition, temperature ...) on the morphology of the polymer films, studied both by AFM and by SAXS. The combination and interpretation of the results obtained by the two techniques are very informative. In the present work, this method was applied to the case of semi-crystalline copolymers, with very atypical behavior and of applicative interest for electroactive devices.

By varying the composition of these terpolymers and the preparation methods (solvent-cast, annealing, melt-crystallized at various cooling rates), it was possible to develop scenarios that explain both the AFM images and the SAXS spectra.

It is concluded that these polymers crystallize with periodically organized lamellae, alternated with amorphous inter-lamellar layers with a long period,  $L_p$ , which is around 14–18 nm depending on the CTFE content, for all the preparation methods studied. To our knowledge, this is the first time that these periodic crystalline stacks have been observed by microscopy after crystallization from the melt.

During annealing in the high temperature phase (paraelectric), a significant growth of the semi-crystalline domains is observed. The thickness of these domains varies between 50 nm and 15 nm for CTFE contents ranging from 0% to 10%.

From the melt, the non-isothermal crystallization takes place in the paraelectric phase. The cooling rates and the CTFE amounts both have

significant influence on the nucleation density which defines the morphologies. Morphologies such as large rectilinear domains, stacks of plates or petals in flowers can be obtained. At room temperature, two periodic stacks would coexist, with periodicities around 30–40 nm and 14–18 nm.

Each morphology has its own ability to orient itself more or less easily on a substrate. This is an advantage for this type of material. Large rectilinear domains formed at low cooling rate and/or low CTFE content have a strong tendency to orient « flat-on » or « edge-on » with respect to the substrate, while small domains obtained after annealing show all possible orientations. Depending on the targeted applications and their associated preparation constraints, one or the other morphology may be chosen to optimize the highly sought-after electroactive properties of these copolymers.

Using the experimental procedure described in this publication, we show how to use SAXS and AFM in parallel to solve both complex evolutions of morphology and to understand atypical SAXS spectra.

#### Author statement

**Sara Zanchi, Sébastien Roland, Sylvie Tencé-Girault:** Conceptualization, Methodology, Writing (Original Draft/Review&Editing), Investigation, Formal analysis. **Marie Engel, Antoine Pascaud, Sylvie Lebreton:** Investigation. **François Bargain:** Writing - Reviewing and Editing. **Fabrice Domingues dos Santos:** Resources, Writing - Reviewing and Editing.

#### Declaration of competing interest

The authors declare that they have no known competing financial interests or personal relationships that could have appeared to influence the work reported in this paper.

#### Data availability

Data will be made available on request.

#### Acknowledgements

This research was carried out within the framework of the Industrial Chair Arkema (Arkema/CNRS-ENSAM-Cnam, Arkema N° AC-2018-413, CNRS N° 183697), authors concerned: all. This work was partially funded by the French National Research Agency (ANR FETA project, ANR-18-CE06-0024), authors concerned: S. Z., A. P., F. D. S., S. R., and S. T-G. We thank the SOLEIL synchrotron facility and the SWING beamline for access to the instrumentation (project n° 20210035). The beamline manager, Javier Perez, is warmly thanked for his advice before and his assistance during the in-situ experiments. The authors gratefully acknowledge the Institut Carnot ARTS for participating in the funding of the PeakForce QNM upgrade of the Multimode AFM microscope used in this study. Finally, Ilias Iliopoulos is thanked for the enlightening discussions as well as for reading and clarifying this manuscript.

#### Appendix A. Supplementary data

Supplementary data to this article can be found online at <https://doi.org/10.1016/j.polymertesting.2023.107973>.

#### References

- [1] X. Chen, X. Han, Q.-D. Shen, PVDF-based ferroelectric polymers in modern flexible electronics, *Adv. Electron. Mater.* 3 (2017), 1600460, <https://doi.org/10.1002/aelm.201600460>.
- [2] S.T. Choi, J.O. Kwon, F. Bauer, Multilayered relaxor ferroelectric polymer actuators for low-voltage operation fabricated with an adhesion-mediated film transfer technique, *Sens. Actuators Phys.* 203 (2013) 282–290, <https://doi.org/10.1016/j.sna.2013.08.049>.

- [3] Q. Jacquemin, Q. Sun, D. Thuau, E. Monteiro, S. Tencé-Girault, N. Mechbal, Design of a new electroactive polymer based continuum actuator for endoscopic surgical robots, *IEEE/RSJ Int. Conf. Intell. Robots Syst. IROS* (2020) 3208–3215, <https://doi.org/10.1109/IROS45743.2020.9341204>, 2020.
- [4] X. Han, X. Chen, X. Tang, Y.-L. Chen, J.-H. Liu, Q.-D. Shen, Flexible polymer transducers for dynamic recognizing physiological signals, *Adv. Funct. Mater.* 26 (2016) 3640–3648, <https://doi.org/10.1002/adfm.201600008>.
- [5] D. Thuau, M. Abbas, G. Wantz, L. Hirsch, I. Dufour, C. Ayela, Piezoelectric polymer gated OFET: cutting-edge electro-mechanical transducer for organic MEMS-based sensors, *Sci. Rep.* 6 (2016), 38672, <https://doi.org/10.1038/srep38672>.
- [6] Z. Hu, M. Tian, B. Nysten, A. Jonas, Regular arrays of highly ordered ferroelectric polymer nanostructures for non-volatile low-voltage memories, *Nat. Mater.* 8 (2009) 62–67, <https://doi.org/10.1038/nmat2339>.
- [7] Y. Zhang, B.R. Aich, S. Chang, K. Lochhead, Y. Tao, How to process P(VDF-TrFE) thin films for controlling short circuits in flexible non-volatile memories, *Org. Electron.* 105 (2022), 106494, <https://doi.org/10.1016/j.orgel.2022.106494>.
- [8] Y. Cho, J.B. Park, B.-S. Kim, J. Lee, W.-K. Hong, I.-K. Park, J.E. Jang, J.I. Sohn, S. Cha, J.M. Kim, Enhanced energy harvesting based on surface morphology engineering of P(VDF-TrFE) film, *Nano Energy* 16 (2015) 524–532, <https://doi.org/10.1016/j.nanoen.2015.07.006>.
- [9] M. Kim, S. Lee, Y. Kim, Solvent-controlled crystalline beta-phase formation in electropun P(VDF-TrFE) fibers for enhanced piezoelectric energy harvesting, *Apl. Mater.* 8 (2020), 071109, <https://doi.org/10.1063/5.0011686>.
- [10] R.G. Kepler, R.A. Anderson, Ferroelectric polymers, *Adv. Phys.* 41 (1992) 1–57, <https://doi.org/10.1080/00018739200101463>.
- [11] L. Yang, B.A. Tyburski, F.D. Dos Santos, M.K. Endoh, T. Koga, D. Huang, Y. Wang, L. Zhu, Relaxor ferroelectric behavior from strong physical pinning in a poly(vinylidene fluoride-co-trifluoroethylene-co-chlorotrifluoroethylene) random terpolymer, *Macromolecules* 47 (2014) 8119–8125, <https://doi.org/10.1021/ma501852x>.
- [12] A.J. Lovinger, Ferroelectric polymers, *Science* 220 (1983) 1115–1121, <https://doi.org/10.1126/science.220.4602.1115>.
- [13] K. Tashiro, M. Kobayashi, Structural phase transition in ferroelectric fluorine polymers: X-ray diffraction and infrared/Raman spectroscopic study, *Phase Transitions* 18 (1989) 213–246, <https://doi.org/10.1080/01411598908206864>.
- [14] L. Zhu, Q. Wang, Novel ferroelectric polymers for high energy density and low loss dielectrics, *Macromolecules* 45 (2012) 2937–2954, <https://doi.org/10.1021/ma2024057>.
- [15] F. Bargain, P. Panine, F. Domingues Dos Santos, S. Tencé-Girault, From solvent-cast to annealed and poled poly(VDF-co-TrFE) films: new insights on the defective ferroelectric phase, *Polymer* 105 (2016) 144–156, <https://doi.org/10.1016/j.polymer.2016.10.010>.
- [16] F. Bargain, D. Thuau, P. Panine, G. Hadzioannou, F. Domingues Dos Santos, S. Tencé-Girault, Thermal behavior of poly(VDF-ter-TrFE-ter-CTFE) copolymers: influence of CTFE monomer on the crystal-crystal transitions, *Polymer* 161 (2019) 64–77, <https://doi.org/10.1016/j.polymer.2018.11.064>.
- [17] T. Furukawa, Ferroelectric properties of vinylidene fluoride copolymers, *Phase Transitions* 18 (1989) 143–211, <https://doi.org/10.1080/01411598908206863>.
- [18] F. Bargain, D. Thuau, G. Hadzioannou, F. Domingues Dos Santos, S. Tencé-Girault, Phase diagram of poly(VDF-ter-TrFE-ter-CTFE) copolymers: relationship between crystalline structure and material properties, *Polymer* 213 (2021), 123203, <https://doi.org/10.1016/j.polymer.2020.123203>.
- [19] W.W. Doll, J.B. Lando, The polymorphism of poly(vinylidene fluoride) IV. The structure of high-pressure-crystallized poly(vinylidene fluoride), *J. Macromol. Sci. Part B* 4 (1970) 889–896, <https://doi.org/10.1080/00222347008217130>.
- [20] P. Pan, Y. Inoue, Polymorphism and isomorphism in biodegradable polyesters, *Prog. Polym. Sci.* 34 (2009) 605–640, <https://doi.org/10.1016/j.progpolymsci.2009.01.003>.
- [21] L. Yang, X. Li, E. Allahyarov, P.L. Taylor, Q.M. Zhang, L. Zhu, Novel polymer ferroelectric behavior via crystal isomorphism and the nanoconfinement effect, *Polymer* 54 (2013) 1709–1728, <https://doi.org/10.1016/j.polymer.2013.01.035>.
- [22] N. María, F. Le Goupil, D. Cavallo, J. Maiz, A.J. Müller, Effect of the TrFE content on the crystallization and SSA thermal fractionation of P(VDF-co-TrFE) copolymers, *Int. J. Mol. Sci.* 23 (2022), 10365, <https://doi.org/10.3390/ijms231810365>.
- [23] K. Tashiro, R. Tanaka, Structural correlation between crystal lattice and lamellar morphology in the ferroelectric phase transition of vinylidene fluoride-trifluoroethylene copolymers as revealed by the simultaneous measurements of wide-angle and small-angle X-ray scatterings, *Polymer* 47 (2006) 5433–5444, <https://doi.org/10.1016/j.polymer.2005.06.128>.
- [24] Y.J. Park, S.J. Kang, C. Park, K.J. Kim, H.S. Lee, M.S. Lee, U.-I. Chung, I.J. Park, Irreversible extinction of ferroelectric polarization in P(VDF-TrFE) thin films upon melting and recrystallization, *Appl. Phys. Lett.* 88 (2006), 242908, <https://doi.org/10.1063/1.2207831>.
- [25] A. Aliane, M. Benwadih, B. Bouthinon, R. Coppard, F. Domingues-Dos Santos, A. Daami, Impact of crystallization on ferro-, piezo- and pyro-electric characteristics in thin film P(VDF-TrFE), *Org. Electron.* 25 (2015) 92–98, <https://doi.org/10.1016/j.orgel.2015.06.007>.
- [26] W. Li, Y. Zhu, D. Hua, P. Wang, X. Chen, J. Shen, Crystalline morphologies of P(VDF-TrFE) (70/30) copolymer films above melting point, *Appl. Surf. Sci.* 254 (2008) 7321–7325, <https://doi.org/10.1016/j.apsusc.2008.05.339>.
- [27] J.S. Lee, A.A. Prabu, K.J. Kim, Annealing effect upon chain orientation, crystalline morphology, and polarizability of ultra-thin P(VDF-TrFE) film for nonvolatile polymer memory device, *Polymer* 51 (2010) 6319–6333, <https://doi.org/10.1016/j.polymer.2010.10.053>.
- [28] D. Guo, I. Stolichnov, N. Setter, Thermally induced cooperative molecular reorientation and nanoscale polarization switching behaviors of ultrathin poly(vinylidene fluoride-trifluoroethylene) films, *J. Phys. Chem. B* 115 (2011) 13455–13466, <https://doi.org/10.1021/jp2061442>.
- [29] J.-H. Kim, D.-Y. Khang, High-performance needle-shaped crystals in thin and ultrathin P(VDF-TrFE) films formed by melt recrystallization, *Eur. Polym. J.* 59 (2014) 78–83, <https://doi.org/10.1016/j.eurpolymj.2014.07.017>.
- [30] J. Hafner, S. Benaglia, F. Richheimer, M. Teuschel, F.J. Maier, A. Werner, S. Wood, D. Platz, M. Schneider, K. Hradil, F.A. Castro, R. Garcia, U. Schmid, Multi-scale characterisation of a ferroelectric polymer reveals the emergence of a morphological phase transition driven by temperature, *Nat. Commun.* 12 (2021) 152, <https://doi.org/10.1038/s41467-020-20407-6>.
- [31] C. Bourgaux-Leonard, J.F. Legrand, A. Renault, P. Delzenne, Annealing effects in ferroelectric poly(vinylidene fluoride-trifluoroethylene) copolymers: real-time studies using synchrotron radiation, *Polymer* 32 (1991) 597–604, [https://doi.org/10.1016/0032-3861\(91\)90470-4](https://doi.org/10.1016/0032-3861(91)90470-4).
- [32] R. Hirose, T. Yoshioka, H. Yamamoto, K.R. Reddy, D. Tahara, K. Hamada, K. Tashiro, In-house simultaneous collection of small-angle X-ray scattering, wide-angle X-ray diffraction and Raman scattering data from polymeric materials, *J. Appl. Crystallogr.* 47 (2014) 922–930, <https://doi.org/10.1107/S1600576714006724>.
- [33] T. Feng, D. Xie, Y. Zang, X. Wu, T. Ren, W. Pan, Temperature control of P(VDF-TrFE) copolymer thin films, *Integrated Ferroelectrics Int. J.* 141 (2013) 187–194, <https://doi.org/10.1080/10584587.2012.694748>.
- [34] I. Katsouras, K. Asadi, M. Li, T.B. van Driel, K.S. Kjær, D. Zhao, T. Lenz, Y. Gu, P.W. M. Blom, D. Damjanovic, M.M. Nielsen, D.M. de Leeuw, The negative piezoelectric effect of the ferroelectric polymer poly(vinylidene fluoride), *Nat. Mater.* 15 (2016) 78–84, <https://doi.org/10.1038/nmat4423>.
- [35] Q. Liu, C. Richard, J.-F. Capsal, Control of crystal morphology and its effect on electromechanical performances of electrostrictive P(VDF-TrFE-CTFE) terpolymer, *Eur. Polym. J.* 91 (2017) 46–60, <https://doi.org/10.1016/j.eurpolymj.2017.03.046>.
- [36] H. Masunaga, S. Sasaki, K. Tashiro, M. Hanesaka, M. Takata, K. Inoue, N. Ohta, N. Yagi, Development of synchrotron DSC/WAXD/SAXS simultaneous measurement system for polymeric materials at the BL40B2 in SPring-8 and its application to the study of crystal phase transitions of fluorine polymers, *Polym. J.* 39 (2007) 1281–1289, <https://doi.org/10.1295/polymj.PJ2007105>.
- [37] D. Qu, J.S. Pedersen, S. Garnier, A. Laschewsky, H. Möhwald, R.v. Klitzing, Effect of polymer charge and geometrical confinement on ion distribution and the structuring in semidilute polyelectrolyte solutions: comparison between AFM and SAXS, *Macromolecules* 39 (2006) 7364–7371, <https://doi.org/10.1021/ma052676q>.
- [38] B. Goderis, H. Reynaers, M.H.J. Koch, Primary and secondary crystallization in a homogeneous ethylene-1-octene copolymer: crystallinity heterogeneity studied by SAXS, *Macromolecules* 35 (2002) 5840–5853, <https://doi.org/10.1021/ma011749c>.
- [39] D.A. Ivanov, S. Hocquet, M. Dosié, M.H.J. Koch, Exploring the melting of a semirigid-chain polymer with temperature-resolved small-angle X-ray scattering, *Eur. Phys. J. E* 13 (2004) 363–378, <https://doi.org/10.1140/epje/i2003-10082-x>.
- [40] G. Reiter, J.-U. Sommer (Eds.), *Polymer Crystallization: Observations, Concepts, and Interpretations*, Springer, Berlin ; New York, 2003.
- [41] T. Gil Haenelt, A. Meyer, C. Abetz, V. Abetz, Planet-like nanostructures formed by an ABC triblock terpolymer, *Macromol. Chem. Phys.* 220 (2019), 1900297, <https://doi.org/10.1002/macp.201900297>.
- [42] J.K. Palacios, A. Tercjak, G. Liu, D. Wang, J. Zhao, N. Hadjichristidis, A.J. Müller, Trilayered morphology of an ABC triple crystalline triblock terpolymer, *Macromolecules* 50 (2017) 7268–7281, <https://doi.org/10.1021/acs.macromol.7b01576>.
- [43] C. Stegelmeier, V. Filiz, V. Abetz, J. Perlich, A. Fery, P. Ruckdeschel, S. Rosenfeldt, S. Förster, Topological paths and transient morphologies during formation of mesoporous block copolymer membranes, *Macromolecules* 47 (2014) 5566–5577, <https://doi.org/10.1021/ma5004908>.
- [44] M.-C. García-Gutiérrez, A. Linares, I. Martín-Fabiani, J.J. Hernández, M. Soccio, D. R. Rueda, T.A. Ezquerro, M. Reynolds, Understanding crystallization features of P(VDF-TrFE) copolymers under confinement to optimize ferroelectricity in nanostructures, *Nanoscale* 5 (2013) 6006–6012, <https://doi.org/10.1039/C3NR00516J>.
- [45] D.J. Blundell, Models for small-angle X-ray scattering from highly dispersed lamellae, *Polymer* 19 (1978) 1258–1266, [https://doi.org/10.1016/0032-3861\(78\)90302-6](https://doi.org/10.1016/0032-3861(78)90302-6).
- [46] S. Sasaki, K. Kubo, A.F.A. Funato, A.C.A. Chiba, Lamellar structure in melted-slowly cooled vinylidene fluoride/trifluoroethylene (86/14) mol% copolymer, *Jpn. J. Appl. Phys.* 35 (1996) 3496, <https://doi.org/10.1143/JJAP.35.3496>.
- [47] S. Sasaki, K. Tashiro, M. Kobayashi, Y. Izumi, K. Kobayashi, Microscopically viewed structural change of PE during the isothermal crystallization from the melt: II. Conformational ordering and lamellar formation mechanism derived from the coupled interpretation of time-resolved SAXS and FTIR data, *Polymer* 40 (1999) 7125–7135, [https://doi.org/10.1016/S0032-3861\(98\)00864-7](https://doi.org/10.1016/S0032-3861(98)00864-7).
- [48] S. Nojima, Y. Kanda, S. Sasaki, Time-Resolved small-angle X-ray scattering studies on the melting behavior of poly( $\epsilon$ -caprolactone)-block-polybutadiene copolymers, *Polym. J.* 30 (1998) 628–634, <https://doi.org/10.1295/polymj.30.628>.
- [49] G.R. Strobl, M. Schneider, Direct evaluation of the electron density correlation function of partially crystalline polymers, *J. Polym. Sci. Polym. Phys. Ed.* 18 (1980) 1343–1359, <https://doi.org/10.1002/pol.1980.180180614>.



- [50] C. Santa Cruz, N. Stribeck, H.G. Zachmann, F.J. Balta Calleja, Novel aspects in the structure of poly(ethylene terephthalate) as revealed by means of small angle x-ray scattering, *Macromolecules* 24 (1991) 5980–5990, <https://doi.org/10.1021/ma00022a013>.
- [51] XSACT: X-ray Scattering Analysis and Calculation Tool. SAXS & WAXS Data Analysis Software Available online: <http://www.xenocs.com/products/software>, n.d.
- [52] M. Wojdyr, Fityk: a general-purpose peak fitting program, *J. Appl. Crystallogr.* 43 (2010) 1126–1128, <https://doi.org/10.1107/S0021889810030499>.
- [53] E. Robelin-Souffache, J. Rault, Origin of the long period and crystallinity in quenched semicrystalline polymers. 1, *Macromolecules* 22 (1989) 3581–3594, <https://doi.org/10.1021/ma00199a015>.
- [54] H. Hama, K. Tashiro, Structural changes in non-isothermal crystallization process of melt-cooled polyoxymethylene[II] evolution of lamellar stacking structure derived from SAXS and WAXS data analysis, *Polymer* 44 (2003) 2159–2168, [https://doi.org/10.1016/S0032-3861\(03\)00093-4](https://doi.org/10.1016/S0032-3861(03)00093-4).
- [55] B.S. Hsiao, K.H. Gardner, D.Q. Wu, B. Chu, Time-resolved X-ray study of poly(aryl ether ether ketone) crystallization and melting behaviour: 2, Melting, *Polymer* 34 (1993) 3996–4003, [https://doi.org/10.1016/0032-3861\(93\)90659-X](https://doi.org/10.1016/0032-3861(93)90659-X).
- [56] H. Matsuda, T. Aoiike, H. Uehara, T. Yamanobe, T. Komoto, Overlapping of different rearrangement mechanisms upon annealing for solution-crystallized polyethylene, *Polymer* 42 (2001) 5013–5021, [https://doi.org/10.1016/S0032-3861\(00\)00893-4](https://doi.org/10.1016/S0032-3861(00)00893-4).